Title

Elevated labile iron in castration-resistant prostate cancer is targetable with ferrous iron-activatable antiandrogen therapy.

Authors

Gonciarz, Ryan
Sakhamuri, Sasank
Hooshdaran, Nima
et al.

Publication Date

2023-03-05

DOI

10.1016/j.ejmech.2023.115110

Peer reviewed

HHS Public Access

Author manuscript

Eur J Med Chem. Author manuscript; available in PMC 2024 March 05.

Published in final edited form as:

Eur J Med Chem. 2023 March 05; 249: 115110. doi:10.1016/j.ejmech.2023.115110.

Elevated Labile Iron in Castration–Resistant Prostate Cancer is Targetable with Ferrous Iron–Activatable Antiandrogen Therapy

Ryan L. Gonciarz[1], **Sasank Sakhamuri**[2], **Nima Hooshdaran**[2], **Garima Kumar**[2], **Hyunjung Kim**[2], **Michael J. Evans**[2,3,*], **Adam R. Renslo**[1,3,*]

[1]Department of Pharmaceutical Chemistry, University of California, San Francisco, San Francisco, California 94158, United States

[2]Department of Radiology and Biomedical Imaging, University of California, San Francisco, San Francisco, California 94158, United States

[3]Helen Diller Family Comprehensive Cancer Center, University of California, San Francisco, San Francisco, California 94158, United States

Abstract

Clinical responses to second generation androgen signaling inhibitors (e.g., enzalutamide) in metastatic castration-resistant prostate cancer (mCRPC) are variable and transient, and are associated with dose limiting toxicities, including rare but severe CNS effects. We hypothesized that changes to iron metabolism coincident with more advanced disease might be leveraged for tumor-selective delivery of antiandrogen therapy. Using the recently described chemical probes SiRhoNox and ^{18}F-TRX in mCRPC models, we found elevated Fe^{2+} to be a common feature of mCRPC *in vitro* and *in vivo*. We next synthesized ferrous-iron activatable drug conjugates of second and third-generation antiandrogens and found these conjugates possessed comparable or enhanced antiproliferative activity across mCRPC cell line models. Mouse pharmacokinetic studies showed that these prototype antiandrogen conjugates are stable *in vivo* and limited exposure to conjugate or free antiandrogen in the brain. Our results reveal elevated Fe^{2+} to be a feature of mCRPC that might be leveraged to improve the tolerability and efficacy of antiandrogen therapy.

Graphical Abstract

[*]**Corresponding Author** Phone: 415-353-3442. Fax: 415-353-9425. michael.evans@ucsf.edu, Phone: 415-514-9698. Fax: 415-514-4507. adam.renslo@ucsf.edu.

Author Contributions

RLG, MJE and ARR conceived research and wrote the manuscript. RLG, SS, GK, and HK performed experiments and analyzed data. MJE and ARR supervised research.

ASSOCIATED CONTENT

Supporting Information file includes Supplementary Figures, additional experimental procedures, and electronic scans of spectral data for final analogs.

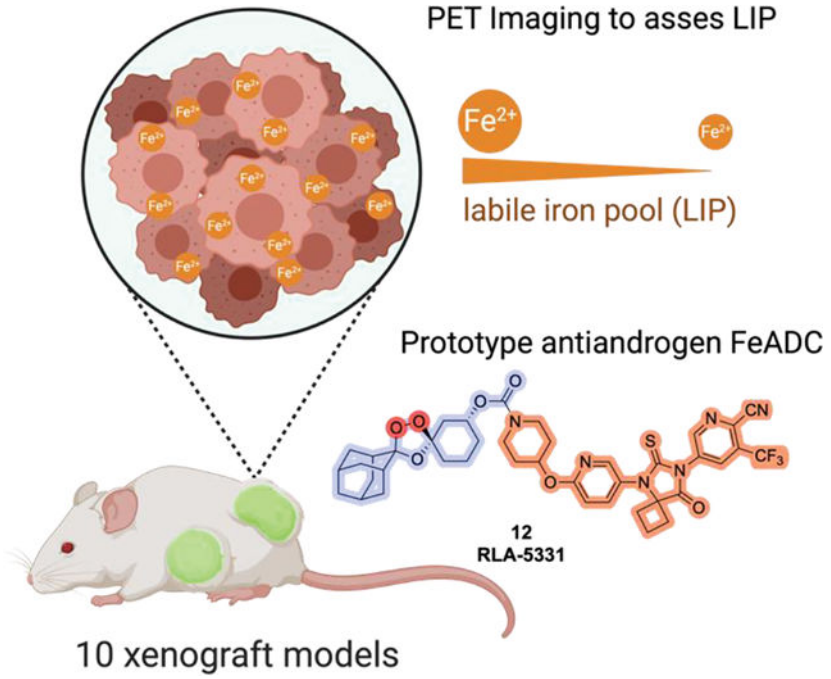

Introduction

Recent advances in antiandrogen therapy have changed the treatment landscape for patients with metastatic castration-resistant prostate cancer (mCRPC), significantly increasing overall survival rates[1,2]. The discovery that androgen receptor (AR) overexpression was a key driver in the progression from castration sensitive disease to mCRPC provided rationale for finding new antiandrogens that could overcome acquired resistance to first-generation antiandrogens, such as bicalutamide[3,4]. This discovery effort led to FDA approved second-generation antiandrogens based on a diarylthiohydantoin core structure including enzalutamide (**1**) and apalutamide (**2**) (Figure 1), that antagonize AR signaling even when AR is highly overexpressed[5,6]. However, treatment responses to these antiandrogens are variable and are often diminished by *de novo* or acquired-resistance to AR antagonism and as such, mCRPC remains uniformly lethal[4,7–9][10,11]. One potential explanation for these incomplete responses are dose limiting toxicities, as the clinical experience with these agents has revealed cognitive effects including mental impairment disorders, dizziness and in rare cases, stroke and seizure[12–14]. One hypothesis regarding these off-target CNS effects involves putative inhibition of γ-aminobutyric acid-gated chloride channels, resulting in lowering of the seizure threshold[15–18]. The development of antiandrogens that can maintain potent inhibition of AR signaling, whilst demonstrating an improved safety profile, remains a major challenge for the field.

Altered iron metabolism in prostate cancer was noted by Torti and co-workers who identified changes to the hepcidin–ferroportin axis responsible for iron export and retention[19,20]. As well, recent pre-clinical and clinical studies of mCRPC using positron emission tomography (PET) and ^{68}Ga citrate or ^{89}Zr-transferrin have revealed links between MYC and mTOR signaling in mCRPC, and increased uptake of ferric iron via the transferrin

receptor[21–24]. Consistent with these studies, ferrous iron-specific probes TRX-PURO[25] and ^{18}F-TRX[26] showed elevated labile iron in PC3 cells *in vitro* and a *Pten*$^{fl/fl}$:*Pb*-Cre prostate cancer model *in vivo*[25–27]. These findings provided the motivation to target such “ferroaddicted” cancer cells with a tumor-activated prodrug[28] strategy we have termed[29] the Fe^{2+}-Activatable Drug Conjugate (FeADC). The FeADC leverages the finely tuned, Fe^{2+}–selective reactivity of antimalarial trioxolanes[30] with a linker that couples the Fenton-type reaction with iron to traceless release of the caged drug payload (Figure 1)[31,32].

Here we used positron emission tomography (PET) with ^{18}F-TRX[26,27] to assess labile iron load in prostate cancer xenograft models spanning a diverse range of genotypes and stages of disease. We describe the new antiandrogen conjugates RLA-4842 and RLA-5331 and explore their antiproliferative activity across mCRPC cell lines, benchmarked against their respective antiandrogen payloads and apalutamide. Finally, we use mouse pharmacokinetic studies to evaluate the potential of the FeADC approach to mitigate free antiandrogen exposure in the brains of mice. Taken together, our cellular, *in vivo* imaging and pharmacokinetic studies revealed an elevation of labile Fe^{2+} in mCRPC tumors compared to less aggressive tumors *in vivo* and suggest the potential of iron-activatable antiandrogen therapy to improve the efficacy and reduce off-target toxicities associated with current treatments.

Results

To evaluate if elevated Fe^{2+} is characteristic of mCRPC, we used the Fe^{2+}-selective fluorescent probe SiRhoNox[33] to compare labile Fe^{2+} levels across a panel of human and mouse prostate cancer cell lines (Figure 2). We normalized the SiRhoNox response of each cell line to that of PC3 cells run concurrently, to allow comparison of experiments performed on different days. We observed significant elevations in Fe^{2+} across most mCPRC cell lines with human AR negative (DU145 and PC3) and enzalutamide-resistant human cell lines ((42F^{ENZR} and 42D^{ENZR})[34] and L’REX[35]) exhibiting relatively higher Fe^{2+} load as compared to AR positive mouse or human adenocarcinoma cell lines (VCaP, LNCaP-AR, C4–2B, 22Rv1, MycCaP and RM1). Next, we evaluated Fe^{2+} load in tumors *in vivo* using ^{18}F-TRX, our previously described[26,27] PET radiotracer for labile iron. We surveyed a total of ten prostate cancer tumor types *in vivo* including prostate adenocarcinoma and small cell neuroendocrine prostate cancer; for reference we included the values of two high-grade glioma models (A172 and U251) we identified previously as harboring low and high Fe^{2+} load, respectively (Figure 2B, 2C). Similar to the *in vitro* studies with SiRhoNox, we found AR-negative tumors (including neuroendocrine-type tumors) tended to stratify towards higher uptake of ^{18}F-TRX. An exception was the bone metastatic model C4–2B, which showed relatively low labile iron load *in vitro*, but high, if variable, uptake of ^{18}F-TRX *in vivo*. Taken together the *in vitro* and *in vivo* imaging data suggest that an elevated pool of Fe^{2+} may be a hallmark of more aggressive, metastatic and treatment-recalcitrant forms of prostate cancer.

We next considered the design and synthesis of prototypical FeADCs bearing antiandrogen payloads. Owing to the absence of suitable conjugation sites/functionality in enzalutamide

(**1**) and apalutamide (**2**), we selected the enzalutamide analogue RD58 (**3**) and the third-generation antiandrogen JNJ-6357625337,38 (**4**) (Figure 1A) as suitable antiandrogen payloads for the synthesis of iron activatable conjugates. A viable linker strategy for **3** was found in the *N,N'*-dimethylethylene-diamine spacer, which we expected would afford stable carbamate linkages to **3** and the caging trioxolane (TRX) moiety. Such di-carbamate linkers have found utility in diverse drug conjugation schemes, including in SYD985, a HER2-targeted antibody-drug conjugate (ADC) currently in phase III clinical trials[36–38]. Thus, compound **3** was synthesized as described[39] and converted to the corresponding *p*-nitrophenylcarbonate intermediate **5**, which was in turn reacted with *N*-Boc *N,N'*-dimethyl-ethylenediamine to afford **6** in yields of 70–74% over two steps (Scheme 1A). Removal of the Boc group produced intermediate **7**, which was reacted with the activated 1,2,4-trioxolane intermediate **8**[40] to afford the desired RD58 conjugate RLA-4842 (**9**). We also synthesized the non-peroxidic, 1,3-dioxolane conjugate RLA-5286 (**11**) (Scheme 1b) as an iron-stable control used to evaluate the effectiveness of RD58 caging, as we have done previously[28] for other FeADCs. Next, we synthesized (*R, R*) and (*S, S*) enantiomeric forms of an FeADC bearing the next-generation antiandrogen **4**. Compound **4** bears an unsubstituted piperidine ring, enabling convenient conjugation via carbamate linkages to enantiomeric trioxolane intermediates (**8** or **13**), to afford the desired conjugates RLA-5331 (**12**) and RLA-5334 (**14**), respectively (Scheme 2**C**).

Prior to testing **9** and **12** in cells, we first confirmed their stability in cell culture media over 72 hr at 37 °C (Supporting Information Figure S1a, b). To study payload release from **9**, we treated the conjugate with ferrous ammonium sulfate (FAS) in a pH neutral buffer at 37 °C and monitored the reaction by UPLC-MS. We observed rapid fragmentation of **9**, followed by formation of the expected intermediates **15** and **16** and finally the free payload **3**, confirming the utility of the di-carbamate linker in the context of an FeADC (Scheme 2). A similar approach was used to verify the Fe^{2+}–dependent activation of **12** and release of its antiandrogen payload **4** (Supporting information, Figure S2a, b).

Antiproliferation Studies and AR Inhibitory Effects of Antiandrogen FeADCs

We next explored the antiproliferative and AR inhibitor effects of **9** and **12** in mCRPC cells exhibiting a ferroaddicted phenotype, as revealed by the cellular and *in vivo* imaging studies described above. We first studied the antiproliferative activity of **9** and its non-peroxidic control conjugate **11** in LNCaP-AR cells, which highly overexpress AR and represent a relevant mechanism of clinical resistance to first-line androgen deprivation therapy (Figure 3a, b). We found that **9** exhibited dose-dependent anti-proliferative effects in LNCaP-AR cells across a concentration range of 0.1–25 μM following three days of drug treatment (Figure 3a). We further found that **9** was substantially more potent than it non-peroxidic (and bioisosteric) control conjugate **11** (Figure 3b). Taken together, these data suggest that the antiandrogen payload **3** present in both **9** and **11** is effectively caged while in the intact FeADC form, and that the anti-proliferative effects of **11** can be attributed to its activation in cells and release of free **3**.

Encouraged by these initial findings, we next explored the antiproliferative activity of **9** as well as **12** across a larger panel of mCRPC cell lines (Figure 4). The comparison

of conjugates **9** and **12** would help establish whether the different linkers and release mechanisms of these two conjugates contribute in unexpected ways to their antiproliferative activity. The growth inhibitory effects of conjugates **9** and **12**, their respective antiandrogen payloads **3** and **4**, and apalutamide (**2**) comparator (Chart 1), were evaluated at a single concentration (5 μM) over 6 days in AR-positive LNCaP, C4–2B, and VCaP cells, and in AR-negative PC3 cells (Figure 4). Interestingly, conjugates **9** and **12** more effectively inhibited the proliferation of LNCaP and C4–2B cells than their respective antiandrogen payloads **3** and **4**. By contrast, parent antiandrogens **3** and **4** were marginally more cytotoxic than **9** and **12** in VCaP cells at day 3 (Figure 4). As expected, none of the conjugates or parent antiandrogens had an anti-proliferative effect in the AR-negative cell line PC3 (Figure 4). Taken together, these data suggested that the antiproliferative effects of **9** and **12** in AR-positive cells derives primarily from release of their antiandrogen payloads and consequent AR inhibition, as expected.

To more directly confirm that compounds **9** and **12** act on target, we performed rt-PCR analysis of the AR-regulated genes kallikrein (KLK-2 and KLK-3) in LNCaP cells (Figure 5). We found that conjugate **9** suppressed the transcription of both AR target genes to a similar degree as the apalutamide positive control, and even more effectively than the conjugate's free antiandrogen payload (**3**). Conjugate **12** also suppressed KLK-2/KLK-3 gene expression relative to vehicle controls, although less effectively than its antiandrogen payload (**4**). The reason for the differential effects of **9** and **12** compared to their respective payloads is presently unclear. Variable effects on AR agonism and antagonism of close structural analogs of antiandrogen payload **4** have been observed in AR functional assays [41]. Thus, it is conceivable that conjugates **9** and **12** exhibit differential activity towards AR in their intact conjugated forms, while their payloads are primarily antagonists. Further studies will be required to determine if intact conjugates **9** or **12** might possess AR agonist activity. Still, the rt-PCR results provided further evidence that both **9** and **12** act on-target at the androgen receptor via release of free antiandrogen payloads **3** and **4** in response to cellular Fe^{2+}.

In Vitro ADME and Pharmacokinetic Profile of Antiandrogen FeADCs

To assess whether the new FeADCs be suitable for study in animal models of mCRPC, both compounds **9**, **12**, and **14** were incubated with mouse (MLM) or human (HLM) liver microsomes (Table 1). We observed a $T_{1/2}$ of 53.4 min (HLM) for **9** and 48.2 min (MLM) for **12**. We found **12** had a slightly improved MLM stability compared to **14**, a trend similar to what we observed with stereoisomeric forms of an earlier FeADC [29]. The kinetic aqueous solubility of **12** and **14** was poor (<0.4 μM), while the solubility of di-carbamate analogue **9** was improved, if still suboptimal (2.3 μM). We next performed pharmacokinetic (PK) studies of **9**, **12**, and apalutamide (**2**) in healthy NSG mice receiving a single 10 mg/kg dose via intraperitoneal (IP) injection (Figure 6a, b and Supporting information Figure S5a). We found the di-carbamate linker present in **9** was mostly stable in plasma, with only ~6% released payload (**3**) detected, relative to **9**, over the course of the experiment (AUC units). Compound **9** had a time to peak plasma concentration (T_{max}) of 0.5 hr with a maximum plasma concentration (C_{max}) of 346 ng/mL (Table 2). Compound **12** showed even better plasma stability, with only ~1% of free payload **4** observed in plasma, and with a T_{max} of

0.5 hr and a higher C_{max} of 641 ng/mL. However, compared to apalutamide (**2**), **9** and **12** exhibited 21- and 14-fold lower overall systemic exposure (AUC) and 12.5- and 6.8-fold lower C_{max} values, respectively (Table 2).

Analysis of the brains of treated mice showed that **9**, **12**, and their respective payloads **3** and **4** showed that **12** and its payload **4** were excluded from brain (**Table 3**, Supporting information, Figure S4), whereas apalutamide treated mice had mean brain concentrations as high as 808 ng/g at the two-hour timepoint (Supporting information, Figure S5b, Table S4). Even considering the 14- to 21-fold higher systemic exposure levels of apalutamide, we conclude that brain exposure as a fraction of total exposure is still reduced in antiandrogen FeADC **12** as compared to apalutamide. Unfortunately, the modest solubilities and exposure profiles of **9** and **12** compared to apalutamide (**2**) make these compounds sub-optimal candidates for *in vivo* pharmacodynamic studies of the FeADC approach in antiandrogen therapy. The identification of conjugates with improved exposure and solubility will be required to meaningfully evaluate their efficacy and potential to mitigate the cognitive and other CNS side effects associated with antiandrogen therapy of mCRPC.

Discussion

Links between altered iron metabolism and tumor growth have previously been established in breast cancer[42,43], glioblastoma[44], prostate cancer[19] and more recently in pancreatic ductal adenocarcinoma[29]. Here, using cutting edge small molecule probes, we performed what is to our knowledge the first significant survey of *in vitro* and *in vivo* Fe^{2+} load across diverse mCRPC cells and tumor models. Finding an elevation of Fe^{2+} in more aggressive mCRPC models, we sought to exploit this iron addicted state with FeADC technology inspired by the iron-dependent pharmacology of antimalarial artemisinins and trioxolanes[45,46].

We synthesized **9**, the first example of an FeADC utilizing a di-carbamate linkage to a phenolic payload (antiandrogen **3**) and confirmed its iron(II)-dependent activation and payload release. We performed initial cellular antiproliferation studies of **9** and dioxolane control **11** in LNCaP-AR cells. We found that **11** lacked any significant cytotoxicity when applied to cells at concentrations at which **9** confers a robust antiproliferative effect (Figure 3B). This confirmed that the antiandrogen payload **3** is caged in its intact FeADC form and furthermore, demonstrated that antiandrogen release from **9** is peroxide-dependent, as expected. We then explored the susceptibility of additional mCRPC cell lines to antiandrogen FeADCs and found that **9** demonstrated more potent antiproliferative activity in AR-positive LNCaP and C4–2B cells than its antiandrogen payload **3** or apalutamide (**2**) at equimolar doses (Figure 4C, 4D). The same effect was observed in LNCaP and C4–2B cells treated with a second FeADC (**12**) based on a different antiandrogen payload (**4**) and distinct mono-carbamate linker (Figure 4C, 4D). In contrast to LNCaP and C4–2B cells, the AR-positive VCaP cell line was marginally more sensitive to the antiandrogen payloads applied directly, than to their FeADC forms. (Figure 4A).

To ascertain the possible contribution of 1,2,4-trioxolane reactivity or byproducts in the activity of **9** and **12**, we employed the AR-negative cell line PC3 which is rich in Fe^{2+}

yet insensitive to the antiandrogens **3** and **4** present in **9** and **12**. We observed a lack of antiproliferative effect for **9** and **12** in PC3 cells (Figure 4B), indicating that iron(II)-promoted reactions of the 1,2,4-trioxolane ring and the byproducts produced therefrom, are insufficient to confer an antiproliferative effect in this AR-negative mCRPC model. We cannot rule out the possibility that reactive oxygen species or side products of trioxolane reactivity do contribute (along with antiandrogen release) to the anti-proliferative effects of **9** and **12** in AR-positive cells. Further studies will be required to explore this possibility and define the relative contributions of such polypharmacology.

We used rt-PCR to show that the expression of AR target genes KLK2 and KLK3 was suppressed by both **9** and **12**, further supporting that these FeADCs release their antiandrogen payloads in mCRPC cell models (Figure 5). Intriguingly, conjugate **9** specifically was shown to inhibit AR transcription more potently than its antiandrogen payload (**3**) applied directly. The fact that the opposite trend was observed for FeADC **12** when compared to its payload **4**, would appear to rule out a contribution of the trioxolane moiety to AR related gene transcription. Instead, we hypothesize that the improved efficacy of **9** may arise from a more extended release of **3** via intermediates **15**/**16** following activation by Fe^{2+}. Slow release of antiandrogen payload may promote enhanced interaction with AR over the course of these experiments, when compared to treatment with a single bolus of antiandrogen payload. Further studies will be required to more fully understand the molecular pharmacology of antiandrogen FeADCs in mCRPC and their temporal effects on AR gene transcription.

We performed PK studies of **9** and **12** in mice and found that both prototypical FeADCs possess good stability *in vivo*, with minimal systemic release of free antiandrogen payloads over the course of several hours. The good *in vivo* stability of di-carbamate **9** is especially encouraging as it suggests the FeADC approach can be extended to phenolic and hydroxyl-bearing payloads more generally. Unfortunately, the overall exposure of **9** and **12** was significantly lower (14- to 21-fold) than for the standard of care antiandrogen apalutamide, suggesting that further *in vivo* optimization of these compounds is warranted prior to their evaluation in mCRPC tumor models. On balance however, our PK studies suggest the potential of an FeADC strategy to minimize antiandrogen exposure in the brain and thereby mitigate their cognitive and other CNS side effects, whilst still promoting their desired antitumor effects via the Fe^{2+}–dependent activation in mCRPC tumors.

Conclusion

Here we found several mCRPC cell lines and *in vivo* tumor models possess significantly elevated levels of Fe^{2+} and that this cell state is targetable with prototypical antiandrogen-bearing FeADCs. We found that antiandrogen FeADCs possessing mechanistically distinct Fe^{2+}-dependent drug-release mechanisms and bearing different AR inhibitor payloads both demonstrated enhanced antiproliferative activity when compared to their respective antiandrogen payloads in two well studied AR-positive mCRPC cell lines. Furthermore, we provided evidence that the antiproliferative effect of these prototype FeADCs is due to on-target inhibition of AR signaling. Finally, we identified the potential of antiandrogen FeADCs to mitigate exposure of intact FeADC and free antiandrogen in the brains of mice.

The discovery of a therapeutically exploitable pool of labile Fe^{2+} in mCPRC cell lines holds promise for next-generation antiandrogen FeADCs that offer superior efficacy and reduced CNS toxicity when treating mCRPC tumors.

Experimental section

General methods.

All compounds tested in cells or animals were >95% pure as determined by UPLC-MS, ^{1}H, ^{13}C and ^{19}F NMR. UPLC-MS compound purity was determined using a Waters Micromass ZQ 4000, equipped with a Waters 2795 Separation Module, Waters 2996 Photodiode Array Detector, and a Waters 2424 ELSD. HPLC was performed on a Waters 2535 Separation Module with a Waters 2998 Photodiode Array Detector. using an XBridge BEH C18, 3.5 μm, 4.6 × 20 mm column, at ambient temperature (unregulated) using a mobile phase of water-methanol containing a constant 0.05% formic acid. (*R*)- and (*S*)- 4-nitrophenyl carbonates and 1,3-dioxolane intermediate (**10**) were prepared as reported previously[47], [28].

The human prostate cancer cell lines LNCaP, C4–2B, 22Rv1, DU145, VCaP, and PC3 were obtained from ATCC and cultured according to the manufacturer's instructions. The mouse prostate cancer cell line RM1 was obtained from ATCC and cultured according to manufacturer's instructions. The mouse prostate cancer cell line MycCaP and the human prostate cancer cell lines LNCaP-AR and L'REX were a generous gift from Dr. Charles Sawyers of MSKCC and cultured as previously described[3,35,48]. The human prostate cancer cell lines 42DENZR and 42FENZR were the generous gift of Dr. Amina Zoubeidi of the Vancouver Prostate Center and were cultured as previously described[34]. Cellular identity was authenticated by visually inspecting morphology and probing for signature expression markers on immunoblot. Mycoplasma contamination was tested within the first two passages after thawing cryostocks with the MycoAlert kit (Lonza). All cells were studied between passages 5 to 25. Patient derived xenografts (PDX) from the LTL series were obtained from Living Tumor Laboratory. The previously described Cas/LN PDX was provided by Dr. Davide Ruggero of UCSF[49]. Enzalutamide and apalutamide were purchased from SelleckChem and used without further purification.

In vitro ADME assays.

Metabolic stability assays performed by Quintara Discovery, Hayward, CA 94545. Compounds were studied at four time points (T = 0, 15, 30, and 60 min) and at 0.5 mg/mL protein concentration, N = 1, + 1 mM NADPH. Percent of parent disappearance is monitored by LC/MS/MS with verapamil as a control. Clearance calculated as (CLint) = $\ln(2)*1000/T_{1/2}$/protein concentration, where protein concentration is in mg/mL. Solubility assessments performed by Analiza, 3615 Superior Ave E, Suite 4407B, Cleveland, OH 44114. Solubility was measured by automated miniaturized shake flask method, with quantitation by chemiluminescent nitrogen detection to measure solubility of compounds from DMSO solutions in phosphate buffered saline, pH 7.4.

RT-PCR Experiments.

Cells were plated on 12 well plates with 1×10^{-6} density per well in three replicates per treatment condition. After 24 hours had passed, drugs were added to the plates at 0.1% final DMSO concentration. Media was removed 48 hours after drug treatment and RNA was extracted (Qiagen, cat#74106). RNA was quantified and 2 μg per sample was transcribed into cDNA (Applied Biosystems, cat#4368813). cDNA was then diluted 1:50 and amplified with 400 nM of primers using a kit (Thermo Scientific, cat#K0252) on a Thermo Pikoreal.

Antiproliferation Assays.

Cancer cells (20,000/well) were seeded four replicates per treatment condition, with 1 mL of 0.1% DMSO complete media into 24-well clear bottom plates. Plates were prepared for drug treatments at 0, 24, 72, and 144 hours. 24 hours post initial seeding, drugs were added to the plates at 0.2% final DMSO concentration. Media was removed after drug treatment, 100 μL of Hanks balanced saline solution buffer and 100 μL of CellTiter-Glo® was added (Promega, cat#G7572). After a 10-minute incubation at room temperature, luminescence was read using a plate reader to assess cell viability (Synergy™ H4 plate reader, BioTek).

FerrofarRed Labile Iron Pool Assay.

Cancer cells (200,000/well) were seeded into 24-well clear-bottom plates. After 24 h, culture media was removed and 100 μL of Hanks balanced saline solution containing FerroFarRed (5 μM; Goryo Chemical) was added into each well and incubated at 37 °C for 50 min. Cells were collected and washed before being placed in HBBS and passed through a cell strainer into FACS tubes. Samples were taken to a flow machine for analysis (FACS CantoII).

PET Imaging Studies.

All animal studies, including housing and welfare monitoring, were conducted in compliance with Institutional Animal Care and Use Committee at UCSF. Animal studies using human prostate cancer cell line xenografts utilized five- to seven-week-old intact male athymic nude mice. Animal studies involving mouse prostate cancer cell line implants utilized immunocompetent five- to seven-week-old C57Bl6 mice. Animal imaging studies involving patient derived xenografts (PDX) utilized eight- to ten-week-old intact male NOD SCID gamma (NSG) mice from Charles River Laboratory. Mice were inoculated subcutaneously (~1.5 ×106 cells) in the flank with a slurry of cells in 1:1 mixture (v/v) of media (DMEM) and Matrigel (Corning). Xenografts were generally palpable within 3–4 weeks after injection. Tumor bearing mice received ~300 μCi of ^{18}F-TRX intravenously. ^{18}F-TRX was prepared as previously described[26]. The tumors were harvested at 90 minutes post injection for biodistribution studies. Blood was harvested via cardiac puncture. Tissues were removed, weighed and counted on a Hidex automatic gamma counter (Turku, Finland). The activity of the injected radiotracer was calculated and used to determine the total number of counts per minute by comparison with a standard of known activity. The data were background- and decay-corrected and expressed as the percentage of the injected dose/weight of the biospecimen in grams (%ID/g).

Synthetic Methods

tert-Butyl (4-(7-(4-cyano-3-(trifluoromethyl)phenyl)-8-oxo-6-thioxo-5,7-diazaspiro[3.4]octan-5-yl)phenyl) ethane-1,2-diylbis(methylcarbamate) (6).

To an Ar(g) purged flask containing antiandrogen **3** (synthesized as reported[39]) (200 mg, 0.479 mmol, 1.0 equiv) was added anhydrous THF (22 mL) and the mixture cooled to 0 °C. 4-Nitrophenyl chloroformate (97.5 mg, 0.484 mmol, 1.0 equiv) and Et_3N (334 μL, 2.40 mmol, 5.0 equiv) were added and the reaction stirred at 0 °C for 2.5 hr. Additional 4-nitrophenyl chloroformate (60.0 mg, 0.298 mmol, 0.62 equiv) was added and the reaction warmed to rt and stirred for 8 hr. Upon formation of activated carbonate intermediate 4-(7-(4-cyano-3-(trifluoromethyl)phenyl)-8-oxo-6-thioxo-5,7-diazaspiro[3.4]octan-5-yl)phenyl (4-nitrophenyl) carbonate (**5**), the reaction was cooled to 0 °C before *tert*-butyl methyl(2-(methylamino)ethyl)carbamate (451 mg, 2.40 mmol, 5.0 equiv) was added dropwise from a separate flask under an Ar(g) atmosphere, the transfer was completed with additional anhydrous THF (2 mL). A color change from pale to bright yellow indicated the nucleophilic displacement of 4-nitrophenol from carbonate **5**. The reaction was stirred for 15 min at 0 °C before UPLC-MS indicated complete consumption of **5**. The reaction mixture was concentrated, resuspended in Et_2O (30 mL) and washed with satd. aq $NaHCO_3$ (7 × 20 mL), brine (1 × 100 mL), dried (MgSO4) and concentrated to a crude residue. Purification via flash column chromatography (80 g silicycle column eluting with 0–60% EtOAc–Hexanes, with the product eluting at 50% EtOAc–Hexanes) afforded *tert*-butyl (4-(7-(4-cyano-3-(trifluoromethyl)phenyl)-8-oxo-6-thioxo-5,7-diazaspiro[3.4]octan-5-yl)phenyl) ethane-1,2-diylbis(methylcarbamate) (**6**) (224.9 mg, 0.479 mmol, 74% (2-step yield)) as a colorless solid. ^{1}H NMR (400 MHz, MeOD) δ 8.15 (s, 1H), 8.13 (s, 1H), 7.98 (dd, J = 8.3, 1.7 Hz, 1H), 7.41 – 7.47 (m, 2H), 7.32 – 7.40 (m, 2H), 3.68 (t, J = 5.4 Hz, 1H), 3.50 – 3.59 (m, 3H), 3.19 (br s, 1H), 3.07 (br s, 2H), 2.91 – 3.01 (m, 3H), 2.53 – 2.70 (m, 4H), 2.02 – 2.23 (m, 1H), 1.56 – 1.68 (m, 1H), 1.41 – 1.55 (m, 9H); ^{13}C NMR (100 MHz, MeOD)[1] δ 180.5, 175.3, 171.6, 156.1, 154.7 (multiple peaks), 152.0 (multiple peaks), 151.9, 138.2, 135.4, 133.0, 132.9, 132.9, 132.7, 132.5, 132.2, 132.2, 131.2, 127.4 (q, $J_{C\text{-}F}$ = 4.4 Hz), 126.4, 125.7, 123.7, 123.0, 122.9, 122.7, 121.0, 115.2, 114.7, 109.1 (d, $J_{C\text{-}F}$ = 2.2 Hz), 80.0, 79.9, 79.8, 79.6, 67.7, 46.7, 46.4, 34.3, 34.2, 33.5, 31.0, 27.4, 13.2, 13.1; ^{19}F NMR (376 MHz, MeOD) δ −63.3; LRMS (ESI): Retention time = 5.50 mins (254 nm), m/z $[M+Na]^+$ calcd for $C_{30}H_{32}F_3N_5O_5SNa$: 654.20, found: 654.09.

[1]Additional peaks in ^{13}C-NMR spectrum of compound **6** are attributed to the slow interconversion of N-Boc and/or *N,N'*-dimethylethylene-diamine rotamers on the NMR timescale.

4-(7-(4-Cyano-3-(trifluoromethyl)phenyl)-8-oxo-6-thioxo-5,7-diazaspiro[3.4]octan-5-yl)phenyl methyl(2-(methylamino)ethyl)carbamate trifluoroacetic acid salt (7).

Intermediate **6** (109.5 mg, 0.173 mmol, 1.0 equiv) was dissolved in CH_2Cl_2 (11.5 mL) and cooled to 0 °C, before TFA (7.5 mL) was added and the mixture stirred at 0 °C for 40 min. Upon completion, the reaction was concentrated under reduced pressure and subjected to azeotropic distillation with toluene (3 × 5 mL). The crude residue was

resuspended in Et_2O and concentrated several times (3 × 10 mL) with sonication to afford 4-(7-(4-cyano-3-(trifluoromethyl)phenyl)-8-oxo-6-thioxo-5,7-diazaspiro[3.4]octan-5-yl)phenyl methyl(2-(methylamino)ethyl)carbamate (**7**) (118.2 mg, 0.183 mmol, quantitative yield) as a colorless free-flowing solid, which was sufficiently pure to be used in the next step without further purification. ^{1}H NMR (400 MHz, MeOD) δ 8.18 (s, 1H), 8.16 (s, 1H), 8.00 (dd, *J* = 8.2, 1.8 Hz, 1H), 7.40 – 7.52 (m, 4H), 3.88 (t, *J* = 5.8 Hz, 1H), 3.76 (t, *J* = 5.6 Hz, 1H), 3.35 – 3.42 (m, 1H), 3.23 (s, 2H), 3.11 (s, 1H), 2.84 (s, 1H), 2.79 (s, 2H), 2.65 – 2.76 (m, 2H), 2.53 – 2.64 (m, 2H), 2.09 – 2.21 (m, 1H), 1.55 – 1.73 (m, 1H); ^{13}C NMR (100 MHz, MeOD) δ 180.5, 175.3, 155.6, 151.9, 151.7, 138.1, 135.4, 133.0, 132.9, 132.5, 132.2, 131.9, 131.2, 131.2, 127.4 (q, $J_{C\text{-}F}$ = 5.1 Hz), 123.7, 122.9, 122.9, 120.9, 114.7, 109.1 (q, $J_{C\text{-}F}$ = 2.2 Hz), 67.7, 47.2, 47.0, 45.7, 45.5, 34.1, 32.7, 32.6, 31.0, 14.1, 13.1; ^{19}F NMR (376 MHz, MeOD) δ −63.5, −77.2 (TFA); LRMS (ESI): Retention time = 4.24 mins (254 nm), m/z $[M+H]^+$ calcd for $C_{25}H_{25}F_3N_5O_3S$: 532.16, found: 532.10.

4-(7-(4-Cyano-3-(trifluoromethyl)phenyl)-8-oxo-6-thioxo-5,7-diazaspiro[3.4]octan-5-yl)phenyl ((1”-*R*, 3”-*R*)-dispiro[adamantane-2,3’-[1,2,4]trioxolane-5’,1”-cyclohexan]-3”-yl) ethane-1,2-diylbis(methylcarbamate) (9).

To an Ar(g) purged vial containing (*R,R*)-dispiro[adamantane-2,3’-[1,2,4]trioxolane-5’,1”-cyclohexan]-3”-yl (4-nitrophenyl) carbonate (**8**)[47] (35 mg, 54 μmol, 1.0 equiv) was added anhydrous DMF (1.2 mL) and Et_3N (19 μL, 0.14 mmol, 2.5 equiv). The mixture was cooled to 0 °C before **7** (12 mg, 27 μmol, 0.5 equiv) was added and the reaction stirred at 0 °C. After 4 hr 40 min, further amine intermediate **7** (14.0 mg, 0.022 mmol, 0.4 equiv) was added, followed by an additional portion of **7** (10.0 mg, 0.015 mmol, 0.29 equiv) at 7 hr. The reaction was stirred at 0 °C for a total of 8 hr before it was passed through a 0.45 μm syringe filter and purified by preparative HPLC (70–85% MeOH–water + 0.05% formic acid over 20 min). The product-bearing fractions were combined, concentrated and washed with DI water (4 × 10 mL) to remove residual formic acid. The organic layer was then concentrated *in vacuo* and lyophilized to give the title compound **9** (16.1 mg, 0.054 mmol, 36%) as a colorless lyophilized solid. ^{1}H NMR (400 MHz, MeOD) δ 8.11 – 8.22 (m, 2H), 8.00 (d, *J* = 8.3 Hz, 1H), 7.46 (d, *J* = 8.3 Hz, 2H), 7.31 – 7.39 (m, 2H), 4.66 – 4.83 (m, 1H), 3.47 – 3.75 (m, 4H), 3.20 (app. d, *J* = 2.7 Hz, 1H), 2.97 – 3.10 (m, 4H), 2.55 – 2.72 (m, 4H), 2.09 – 2.34 (m, 2H), 1.87 – 2.03 (m, 8H), 1.70 – 1.85 (m, 10H), 1.57 – 1.69 (m, 2H), 1.34 – 1.55 (m, 3H); ^{13}C NMR (100 MHz, MeOD)[1] δ 180.5, 175.4, 156.1, 154.7, 151.9, 138.2, 138.1, 135.3, 133.0, 132.9, 132.8, 132.8, 132.5, 132.2, 131.3, 131.2, 127.4 (q, $J_{C\text{-}F}$ = 5.14 Hz), 123.7, 123.0, 122.8, 122.7, 122.7, 121.0, 114.6, 111.3, 111.3, 109.2, 108.6, 108.6, 108.5, 72.0, 71.8, 71.8, 71.7, 67.7, 46.5 (multiple peaks), 46.2, 45.8, 45.7, 39.8, 39.7, 39.6, 39.5, 36.4, 36.4, 36.3, 34.4, 34.2, 34.2, 34.0, 33.8, 33.6, 33.6, 33.4, 33.4, 33.3, 31.0, 30.3, 30.2, 29.3, 26.9, 26.5, 19.5, 19.4, 19.3, 19.3, 19.2, 13.1, 13.1; ^{19}F NMR (376 MHz, MeOD) δ −63.5; LRMS (ESI): Retention time = 6.42 mins (254 nm), HRMS (ESI): m/z $[M+Na]^+$ calcd for $C_{42}H_{46}F_3N_5O_8SNa^+$: 860.2911, found: 860.2915.

[1]Additional peaks in ^{13}C-NMR spectrum of compound **9** are attributed to the slow interconversion of *N,N’*-dimethylethylene-diamine rotamers on the NMR timescale.

4-(7-(4-Cyano-3-(trifluoromethyl)phenyl)-8-oxo-6-thioxo-5,7-diazaspiro[3.4]octan-5-yl)phenyldispiro[adamantane-2,4'-[1,3]dioxolane-2',1"-cyclohexan]-3"-yl) ethane-1,2-diylbis(methylcarbamate) (11).

To an Ar(g) purged vial containing dispiro[adamantane-2,4'-[1,3]dioxolane-2',1"-cyclohexan]-3"-yl (4-nitrophenyl) carbonate (**10**) (30 mg, 0.046 mmol, 1.0 equiv) was added anhydrous DMF (1.2 mL) and Et_3N (16 μL, 0.12 mmol, 2.5 equiv). The mixture was cooled to 0 °C before amine intermediate **7** (12 mg, 27 μmol, 0.5 equiv) was added and the reaction stirred at 0 °C. After 4 hr 40 min, further intermediate **7** (6.0 mg, 0.09 mmol, 0.4 equiv) was added in anhydrous DMF (400 μL) and the reaction warmed to between 0–5 °C for 5 hr. Upon completion, the crude reaction mixture was passed through a 0.45 μm syringe filter and purified by preparative HPLC (70–85% MeOH–water + 0.05% formic acid over 20 min). The product-bearing fractions were combined, concentrated and washed with DI water (4 × 10 mL) to remove residual formic acid. The organic layer was then concentrated and lyophilized to give the title compound **11** (9.3 mg, 0.011 mmol, 24%) as a colorless lyophilized solid. ^{1}H NMR (400 MHz, MeOD) δ 8.17 (dd, J = 4.7, 3.3 Hz, 2H), 8.00 (dd, J = 8.3, 1.7 Hz, 1H), 7.45 (d, J = 8.5 Hz, 2H), 7.31 – 7.40 (m, 2H), 3.80 – 3.95 (m, 2H), 3.40 – 3.79 (m, 4H), 3.19 (s, 1H), 2.96 – 3.07 (m, 5H), 2.54 – 2.74 (m, 4H), 2.05 – 2.30 (m, 4H), 1.85 – 2.00 (m, 1H), 1.70 – 1.84 (m, 9H), 1.56 – 1.69 (m, 8H), 1.34 – 1.54 (m, 3H); ^{13}C NMR (100 MHz, MeOD)[1] δ 180.5, 175.4, 156.1, 154.7, 151.9, 138.2, 135.3, 133.0, 132.8, 132.5, 132.2, 131.3, 131.2, 127.4 (q, $J_{C\text{-}F}$ = 5.1 Hz), 126.4, 123.7, 123.1, 122.8, 122.7, 121.0, 114.6, 111.3, 111.3, 109.2 (q, $J_{C\text{-}F}$ = 2.2 Hz), 108.7, 108.7, 84.8 (multiple peaks), 84.5, 73.0, 72.8, 72.0, 72.0, 67.7, 46.5, 46.6 (multiple peaks), 46.4, 46.1, 45.7 (multiple peaks), 42.6, 42.5, 37.4, 37.3, 37.3, 37.1, 35.9, 35.4, 35.4, 34.2, 34.1, 33.9, 33.6, 33.5, 33.4, 33.3, 33.2, 31.0, 30.9, 30.9, 27.1, 26.8, 26.5, 19.7, 19.5, 13.1, 13.1, 39.8, 39.7, 39.6, 39.5, 36.4, 36.4, 36.3, 34.4, 34.2, 34.0, 33.8, 33.6, 33.4, 33.3, 31.0, 30.3, 30.2, 26.9, 26.5, 19.5, 19.4, 19.3, 19.3, 19.2, 13.1, 13.1; ^{19}F NMR (376 MHz, MeOD) δ −63.5; LRMS (ESI): Retention time = 6.34 mins (254 nm); HRMS (ESI): m/z $[M+Na]^+$ calcd for $C_{43}H_{48}F_3N_5O_7SNa^+$: 858.3119, found: 858.3115.

[1]Additional peaks in ^{13}C-NMR spectrum of compound **11** are attributed to the slow interconversion of *N,N'*-dimethylethylene-diamine rotamers on the NMR timescale.

(1"-*R*, 3"-*R*)-Dispiro[adamantane-2,3'-[1,2,4]trioxolane-5',1"-cyclohexan]-3"-yl 4-((5-(7-(6-cyano-5-(trifluoromethyl)pyridin-3-yl)-8-oxo-6-thioxo-5,7-diazaspiro[3.4]octan-5-yl)pyridin-2-yl)oxy)piperidine-1-carboxylate (12).

To an Ar(g) purged vial containing JNJ-63576253 as the TFA salt (synthesized as reported[50] or purchased from MedChemExpress as a HCl salt (Cat #. HY-115282A, 288 mg, 0.436 mmol, 1.0 equiv) was added anhydrous DMF (1.2 mL) and *i*-Pr_2NEt (379 μL, 2.18 mmol, 5.0 equiv). The mixture was cooled to 0 °C before intermediate **8** (213 mg, 0.479 mmol, 1.1 equiv) was added and the reaction allowed to gradually warm to rt and stirred for 16 hr. Upon completion, the reaction was diluted with EtOAc (30 mL) and washed with satd. $NaHCO_3$ (10 × 20 mL). The aqueous layer was extracted with EtOAc (150 mL) and the organic layers were combined, washed with brine (200 mL), dried ($MgSO_4$), filtered, and concentrated to a crude residue. Purification via column chromatography (12 g silicycle column eluting with 0–30% EtOAc–Hexanes, with the

product eluting at 23% EtOAc–Hexanes) afforded the title compound **12** (349.8 mg, 0.433 mmol, 99%) as a colorless solid. ^{1}H NMR (400 MHz, $CDCl_3$) δ 9.10 (s, 1H), 8.37 (s, 1H), 8.10 (s, 1H), 7.53 (dd, *J* = 8.6, 2.1 Hz, 1H), 6.92 (d, *J* = 8.8 Hz, 1H), 5.31 (br s, 1H), 4.74 – 4.87 (m, 1H), 3.72 – 3.93 (m, 2H), 3.37 (br s, 2H), 2.66 – 2.77 (m, 2H), 2.45 – 2.60 (m, 2H), 2.08 – 2.33 (m, 4H), 1.69 – 2.10 (m, 21H), 1.47 – 1.63 (m, 2H), 1.34 – 1.46 (m, 1H); ^{13}C NMR (100 MHz, $CDCl_3$) δ 210.9, 179.9, 174.4, 163.4, 154.7, 152.3, 147.8, 140.1, 134.0 (q, J_{C-F} = 4.7 Hz**),** 132.4, 130.6, 130.3, 129.9, 125.1, 122.7, 119.9, 113.8, 113.0, 111.6, 108.6, 71.3, 71.2, 69.5, 67.5, 53.8, 41.1, 39.8, 36.8, 36.3, 36.3, 34.9, 34.8, 34.7, 34.6, 34.1, 31.8, 31.6, 30.9, 29.3, 26.9, 26.5, 19.6, 13.7; ^{19}F NMR (376 MHz, $CDCl_3$) δ −61.87; LRMS (ESI): Retention time = 6.70 mins (254 nm); HRMS (ESI negative mode): m/z $[M+Cl]^-$ calcd for $C_{40}H_{43}F_3N_6O_7SCl^-$: 843.2560, found: 843.2581.

(1”-*S*, 3”-*S*)-Dispiro[adamantane-2,3’-[1,2,4]trioxolane-5’,1”-cyclohexan]-3”-yl 4-((5-(7-(6-cyano-5-(trifluoromethyl)pyridin-3-yl)-8-oxo-6-thioxo-5,7-diazaspiro[3.4]octan-5-yl)pyridin-2-yl)oxy)piperidine-1-carboxylate (14).

Prepared as described for **12** but using (*S, S*)-dispiro[adamantane-2,3’-[1,2,4]trioxolane-5’,1”-cyclohexan]-3”-yl (4-nitrophenyl) carbonate (**13**)[47] to afford the title compound **14** (40.8 mg, 0.05 mmol, 90%) as a colorless solid. ^{1}H NMR (400 MHz, $CDCl_3$) δ 9.10 (d, *J* = 1.9 Hz, 1H), 8.37 (d, *J* = 1.9 Hz, 1H), 8.10 (d, *J* = 2.4 Hz, 1H), 7.53 (dd, *J* = 8.8, 2.7 Hz, 1H), 6.92 (d, *J* = 8.8 Hz, 1H), 5.31 (dt, *J* = 7.5, 3.9 Hz, 1H), 4.75 – 4.89 (m, 1H), 3.74 – 3.93 (m, 2H), 3.31 – 3.42 (m, 2H), 2.66 – 2.79 (m, 2H), 2.47 – 2.59 (m, 2H), 2.15 – 2.37 (m, 3H), 1.69 – 2.09 (m, 22H), 1.48 – 1.64 (m, 2H), 1.31 – 1.45 (m, 1H); ^{13}C NMR (100 MHz, $CDCl_3$) δ 210.9, 179.9, 174.4, 163.4, 154.7, 152.3, 147.8, 140.1, 134.0 (q, J_{C-F} = 4.2 Hz), 132.3, 130.6, 130.3, 130.0, 129.9, 125.1, 122.7, 119.9, 113.8, 113.0, 111.7, 108.7, 71.3, 71.2, 69.5, 67.5, 53.8, 41.1, 39.9, 36.8, 36.7, 36.3, 36.3, 35.0, 34.8, 34.7, 34.6, 34.1, 31.8, 31.6, 29.3, 26.9, 26.5, 24.7, 19.6, 13.7; ^{19}F NMR (376 MHz, $CDCl_3$) δ −61.87; LRMS (ESI): Retention time = 6.70 mins (254 nm); HRMS (ESI negative mode): m/z $[M+Cl]^-$ calcd for $C_{40}H_{43}F_3N_6O_7SCl^-$: 843.2560, found: 843.2571.

Supplementary Material

Refer to Web version on PubMed Central for supplementary material.

ACKNOWLEDGMENT

We thank the Preclinical Therapeutics Core at UCSF Helen Diller Comprehensive Cancer Center for assistance with animal pharmacokinetic studies.

Funding Sources

ARR acknowledges funding from National Institutes of Health (R01 AI105106 and R01 CA260860), the Congressionally Directed Medical Research Programs (W81XWH1810754) and the UCSF Benioff Initiative for Prostate Cancer Research. MJE acknowledges funding from an American Cancer Society Research Scholar Grant (130635-RSG-1 7–005-01-CCE), an American Cancer Society Mission Boost Grant (MBGI-21–180-01-MBG), the National Institute of Biomedical Imaging and Bioengineering (R01EB029429), the Congressionally Directed Medical Research Programs (W81XWH1810763) and the UCSF Benioff Initiative for Prostate Cancer Research.

BIBLIOGRAPHY

[1]. Tucci M, Scagliotti GV, Vignani F, Metastatic castration-resistant prostate cancer: time for innovation., Future Oncol. 11 (2015) 91–106. 10.2217/fon.14.145. [PubMed: 25572785]

[2]. Kirby M, Hirst C, Crawford ED, Characterising the castration-resistant prostate cancer population: a systematic review., Int. J. Clin. Pract. 65 (2011) 1180–1192. 10.1111/j.1742-1241.2011.02799.x. [PubMed: 21995694]

[3]. Chen CD, Welsbie DS, Tran C, Baek SH, Chen R, Vessella R, Rosenfeld MG, Sawyers CL, Molecular determinants of resistance to antiandrogen therapy., Nat. Med. 10 (2004) 33–39. 10.1038/nm972. [PubMed: 14702632]

[4]. Watson PA, Arora VK, Sawyers CL, Emerging mechanisms of resistance to androgen receptor inhibitors in prostate cancer., Nat. Rev. Cancer. 15 (2015) 701–711. 10.1038/nrc4016. [PubMed: 26563462]

[5]. Clegg NJ, Wongvipat J, Joseph JD, Tran C, Ouk S, Dilhas A, Chen Y, Grillot K, Bischoff ED, Cai L, Aparicio A, Dorow S, Arora V, Shao G, Qian J, Zhao H, Yang G, Cao C, Sensintaffar J, Wasielewska T, Herbert MR, Bonnefous C, Darimont B, Scher HI, Smith-Jones P, Klang M, Smith ND, De Stanchina E, Wu N, Ouerfelli O, Rix PJ, Heyman RA, Jung ME, Sawyers CL, Hager JH, ARN-509: a novel antiandrogen for prostate cancer treatment., Cancer Res. 72 (2012) 1494–1503. 10.1158/0008-5472.CAN-11-3948. [PubMed: 22266222]

[6]. Tran C, Ouk S, Clegg NJ, Chen Y, Watson PA, Arora V, Wongvipat J, Smith-Jones PM, Yoo D, Kwon A, Wasielewska T, Welsbie D, Chen CD, Higano CS, Beer TM, Hung DT, Scher HI, Jung ME, Sawyers CL, Development of a second-generation antiandrogen for treatment of advanced prostate cancer., Science. 324 (2009) 787–790. 10.1126/science.1168175. [PubMed: 19359544]

[7]. Henríquez I, Roach M, Morgan TM, Bossi A, Gómez JA, Abuchaibe O, Couñago F, Current and Emerging Therapies for Metastatic Castration-Resistant Prostate Cancer (mCRPC)., Biomedicines. 9 (2021). 10.3390/biomedicines9091247.

[8]. Hussain M, Mateo J, Fizazi K, Saad F, Shore N, Sandhu S, Chi KN, Sartor O, Agarwal N, Olmos D, Thiery-Vuillemin A, Twardowski P, Roubaud G, Özgüroğlu M, Kang J, Burgents J, Gresty C, Corcoran C, Adelman CA, de Bono J, PROfound Trial Investigators, Survival with Olaparib in Metastatic Castration-Resistant Prostate Cancer., N. Engl. J. Med. 383 (2020) 2345–2357. 10.1056/NEJMoa2022485. [PubMed: 32955174]

[9]. Scher HI, Solo K, Valant J, Todd MB, Mehra M, Prevalence of prostate cancer clinical states and mortality in the united states: estimates using a dynamic progression model., PLoS ONE. 10 (2015) e0139440. 10.1371/journal.pone.0139440. [PubMed: 26460686]

[10]. Chen Y, Zhou Q, Hankey W, Fang X, Yuan F, Second generation androgen receptor antagonists and challenges in prostate cancer treatment., Cell Death Dis. 13 (2022) 632. 10.1038/s41419-022-05084-1. [PubMed: 35864113]

[11]. Buttigliero C, Tucci M, Bertaglia V, Vignani F, Bironzo P, Di Maio M, Scagliotti GV, Understanding and overcoming the mechanisms of primary and acquired resistance to abiraterone and enzalutamide in castration resistant prostate cancer., Cancer Treat. Rev. 41 (2015) 884–892. 10.1016/j.ctrv.2015.08.002. [PubMed: 26342718]

[12]. Higano CS, Beer TM, Taplin M-E, Efstathiou E, Hirmand M, Forer D, Scher HI, Long-term Safety and Antitumor Activity in the Phase 1–2 Study of Enzalutamide in Pre- and Post-docetaxel Castration-Resistant Prostate Cancer., Eur. Urol. 68 (2015) 795–801. 10.1016/j.eururo.2015.01.026. [PubMed: 25698064]

[13]. Pilon D, Behl AS, Ellis LA, Robitaille M-N, Lefebvre P, Dawson NA, Assessment of Real-World Central Nervous System Events in Patients with Advanced Prostate Cancer Using Abiraterone Acetate, Bicalutamide, Enzalutamide, or Chemotherapy., Am. Health Drug Benefits. 10 (2017) 143–153. [PubMed: 28626511]

[14]. Smith MR, Saad F, Chowdhury S, Oudard S, Hadaschik BA, Graff JN, Olmos D, Mainwaring PN, Lee JY, Uemura H, Lopez-Gitlitz A, Trudel GC, Espina BM, Shu Y, Park YC, Rackoff WR, Yu MK, Small EJ, SPARTAN Investigators, Apalutamide Treatment and Metastasis-free Survival in Prostate Cancer., N. Engl. J. Med. 378 (2018) 1408–1418. 10.1056/NEJMoa1715546. [PubMed: 29420164]

[15]. Moilanen A-M, Riikonen R, Oksala R, Ravanti L, Aho E, Wohlfahrt G, Nykänen PS, Törmäkangas OP, Palvimo JJ, Kallio PJ, Discovery of ODM-201, a new-generation androgen receptor inhibitor targeting resistance mechanisms to androgen signaling-directed prostate cancer therapies., Sci. Rep. 5 (2015) 12007. 10.1038/srep12007. [PubMed: 26137992]

[16]. Foster WR, Car BD, Shi H, Levesque PC, Obermeier MT, Gan J, Arezzo JC, Powlin SS, Dinchuk JE, Balog A, Salvati ME, Attar RM, Gottardis MM, Drug safety is a barrier to the discovery and development of new androgen receptor antagonists., Prostate. 71 (2011) 480–488. 10.1002/pros.21263. [PubMed: 20878947]

[17]. Treiman DM, GABAergic mechanisms in epilepsy., Epilepsia. 42 Suppl 3 (2001) 8–12. 10.1046/j.1528-1157.2001.042suppl.3008.x. [PubMed: 11520315]

[18]. Ryan C, Wefel JS, Morgans AK, A review of prostate cancer treatment impact on the CNS and cognitive function., Prostate Cancer Prostatic Dis. 23 (2020) 207–219. 10.1038/s41391-019-0195-5. [PubMed: 31844181]

[19]. Tesfay L, Clausen KA, Kim JW, Hegde P, Wang X, Miller LD, Deng Z, Blanchette N, Arvedson T, Miranti CK, Babitt JL, Lin HY, Peehl DM, Torti FM, Torti SV, Hepcidin regulation in prostate and its disruption in prostate cancer., Cancer Res. 75 (2015) 2254–2263. 10.1158/0008-5472.CAN-14-2465. [PubMed: 25858146]

[20]. Deng Z, Manz DH, Torti SV, Torti FM, Effects of Ferroportin-Mediated Iron Depletion in Cells Representative of Different Histological Subtypes of Prostate Cancer., Antioxid. Redox Signal. 30 (2019) 1043–1061. 10.1089/ars.2017.7023. [PubMed: 29061069]

[21]. Aggarwal R, Behr SC, Paris PL, Truillet C, Parker MFL, Huynh LT, Wei J, Hann B, Youngren J, Huang J, Premasekharan G, Ranatunga N, Chang E, Gao KT, Ryan CJ, Small EJ, Evans MJ, Real-Time Transferrin-Based PET Detects MYC-Positive Prostate Cancer., Mol. Cancer Res. 15 (2017) 1221–1229. 10.1158/1541-7786.MCR-17-0196. [PubMed: 28592703]

[22]. Behr SC, Aggarwal R, Seo Y, Aparici CM, Chang E, Gao KT, Tao DH, Small EJ, Evans MJ, A feasibility study showing [68ga]citrate PET detects prostate cancer., Mol. Imaging Biol. 18 (2016) 946–951. 10.1007/s11307-016-0966-5. [PubMed: 27184068]

[23]. Truillet C, Cunningham JT, Parker MFL, Huynh LT, Conn CS, Ruggero D, Lewis JS, Evans MJ, Noninvasive Measurement of mTORC1 Signaling with 89Zr-Transferrin., Clin. Cancer Res. 23 (2017) 3045–3052. 10.1158/1078-0432.CCR-16-2448. [PubMed: 28007777]

[24]. Holland JP, Evans MJ, Rice SL, Wongvipat J, Sawyers CL, Lewis JS, Annotating MYC status with 89Zr-transferrin imaging., Nat. Med. 18 (2012) 1586–1591. 10.1038/nm.2935. [PubMed: 23001181]

[25]. Spangler B, Morgan CW, Fontaine SD, Vander Wal MN, Chang CJ, Wells JA, Renslo AR, A reactivity-based probe of the intracellular labile ferrous iron pool., Nat. Chem. Biol. 12 (2016) 680–685. 10.1038/nchembio.2116. [PubMed: 27376690]

[26]. Muir RK, Zhao N, Wei J, Wang Y-H, Moroz A, Huang Y, Chen Y-C, Sriram R, Kurhanewicz J, Ruggero D, Renslo AR, Evans MJ, Measuring Dynamic Changes in the Labile Iron Pool in Vivo with a Reactivity-Based Probe for Positron Emission Tomography., ACS Cent. Sci. 5 (2019) 727–736. 10.1021/acscentsci.9b00240. [PubMed: 31041393]

[27]. Zhao N, Huang Y, Wang Y-H, Muir RK, Chen Y-C, Wei J, Hooshdaran N, Viswanath P, Seo Y, Ruggero D, Renslo AR, Evans MJ, Ferronostics: Measuring Tumoral Ferrous Iron with PET to Predict Sensitivity to Iron-Targeted Cancer Therapies., J. Nucl. Med. 62 (2021) 949–955. 10.2967/jnumed.120.252460. [PubMed: 33246980]

[28]. Spangler B, Fontaine SD, Shi Y, Sambucetti L, Mattis AN, Hann B, Wells JA, Renslo AR, A Novel Tumor-Activated Prodrug Strategy Targeting Ferrous Iron Is Effective in Multiple Preclinical Cancer Models., J. Med. Chem. 59 (2016) 11161–11170. 10.1021/acs.jmedchem.6b01470. [PubMed: 27936709]

[29]. Jiang H, Muir RK, Gonciarz RL, Olshen AB, Yeh I, Hann BC, Zhao N, Wang Y-H, Behr SC, Korkola JE, Evans MJ, Collisson EA, Renslo AR, Ferrous iron-activatable drug conjugate achieves potent MAPK blockade in KRAS-driven tumors., J. Exp. Med. 219 (2022). 10.1084/jem.20210739.

[30]. Creek DJ, Charman WN, Chiu FCK, Prankerd RJ, McCullough KJ, Dong Y, Vennerstrom JL, Charman SA, Iron-mediated degradation kinetics of substituted dispiro-1,2,4-trioxolane antimalarials., J. Pharm. Sci. 96 (2007) 2945–2956. 10.1002/jps.20958. [PubMed: 17549767]

[31]. Fontaine SD, DiPasquale AG, Renslo AR, Efficient and stereocontrolled synthesis of 1,2,4-trioxolanes useful for ferrous iron-dependent drug delivery., Org. Lett. 16 (2014) 5776–5779. 10.1021/ol5028392. [PubMed: 25331549]

[32]. Fontaine SD, Spangler B, Gut J, Lauterwasser EMW, Rosenthal PJ, Renslo AR, Drug delivery to the malaria parasite using an arterolane-like scaffold., ChemMedChem. 10 (2015) 47–51. 10.1002/cmdc.201402362. [PubMed: 25314098]

[33]. Hirayama T, Tsuboi H, Niwa M, Miki A, Kadota S, Ikeshita Y, Okuda K, Nagasawa H, A universal fluorogenic switch for Fe(ii) ion based on N-oxide chemistry permits the visualization of intracellular redox equilibrium shift towards labile iron in hypoxic tumor cells., Chem. Sci. 8 (2017) 4858–4866. 10.1039/c6sc05457a. [PubMed: 28959409]

[34]. Bishop JL, Thaper D, Vahid S, Davies A, Ketola K, Kuruma H, Jama R, Nip KM, Angeles A, Johnson F, Wyatt AW, Fazli L, Gleave ME, Lin D, Rubin MA, Collins CC, Wang Y, Beltran H, Zoubeidi A, The Master Neural Transcription Factor BRN2 Is an Androgen Receptor-Suppressed Driver of Neuroendocrine Differentiation in Prostate Cancer., Cancer Discov. 7 (2017) 54–71. 10.1158/2159-8290.CD-15-1263. [PubMed: 27784708]

[35]. Arora VK, Schenkein E, Murali R, Subudhi SK, Wongvipat J, Balbas MD, Shah N, Cai L, Efstathiou E, Logothetis C, Zheng D, Sawyers CL, Glucocorticoid receptor confers resistance to antiandrogens by bypassing androgen receptor blockade., Cell. 155 (2013) 1309–1322. 10.1016/j.cell.2013.11.012. [PubMed: 24315100]

[36]. Branch JR, Bush TL, Pande V, Connolly PJ, Zhang Z, Hickson I, Ondrus J, Jaensch S, Bischoff JR, Habineza G, Van Hecke G, Meerpoel L, Packman K, Parrett CJ, Chong YT, Gottardis MM, Bignan G, Discovery of JNJ-63576253, a Next-Generation Androgen Receptor Antagonist Active Against Wild-Type and Clinically Relevant Ligand Binding Domain Mutations in Metastatic CastrationResistant Prostate Cancer, Mol. Cancer Ther. 20 (2021) 763–774. [PubMed: 33649102]

[37]. Elgersma RC, Coumans RGE, Huijbregts T, Menge WMPB, Joosten JAF, Spijker HJ, de Groot FMH, van der Lee MMC, Ubink R, van den Dobbelsteen DJ, Egging DF, Dokter WHA, Verheijden GFM, Lemmens JM, Timmers CM, Beusker PH, Design, Synthesis, and Evaluation of Linker-Duocarmycin Payloads: Toward Selection of HER2-Targeting Antibody-Drug Conjugate SYD985., Mol. Pharm. 12 (2015) 1813–1835. 10.1021/mp500781a. [PubMed: 25635711]

[38]. BioSpace, Byondis announces positive topline results of pivotal phase III TULIP® study in patientswith HER2-positive unresectable locally advanced or metastatic breast cancer. News release. Byondis BV June 8, 2021., (2021). https://www.biospace.com/article/releases/byondis-announces-positive-topline-results-of-pivotal-phase-iii-tulip-study-in-patients-with-her2-positive-unresectable-locally-advanced-or-metastatic-breast-cancer/ (accessed April 30, 2022).

[39]. Sawyers CL, Jung ME, Chen CD, Ouk S, Tran C, Wongvipat J, Yoo D, Diarylhydantoin compounds. U.S. Patent 7,709,517., US7709517B2 (A1), 2010.

[40]. Lauterwasser EMW, Fontaine SD, Li H, Gut J, Katneni K, Charman SA, Rosenthal PJ, Bogyo M, Renslo AR, Trioxolane-Mediated Delivery of Mefloquine Limits Brain Exposure in a Mouse Model of Malaria., ACS Med. Chem. Lett. 6 (2015) 1145–1149. 10.1021/acsmedchemlett.5b00296. [PubMed: 26617969]

[41]. Smith ND, Bonnefous C, Julien JD, Androgen receptor modulators and uses thereof, WO 2011/103202 A2, 2011.

[42]. Miller LD, Coffman LG, Chou JW, Black MA, Bergh J, D'Agostino R, Torti SV, Torti FM, An iron regulatory gene signature predicts outcome in breast cancer., Cancer Res. 71 (2011) 6728–6737. 10.1158/0008-5472.CAN-11-1870. [PubMed: 21875943]

[43]. Pinnix ZK, Miller LD, Wang W, D'Agostino R, Kute T, Willingham MC, Hatcher H, Tesfay L, Sui G, Di X, Torti SV, Torti FM, Ferroportin and iron regulation in breast cancer progression and prognosis., Sci. Transl. Med. 2 (2010) 43ra56. 10.1126/scisignal.3001127.

[44]. Schonberg DL, Miller TE, Wu Q, Flavahan WA, Das NK, Hale JS, Hubert CG, Mack SC, Jarrar AM, Karl RT, Rosager AM, Nixon AM, Tesar PJ, Hamerlik P, Kristensen BW, Horbinski C, Connor JR, Fox PL, Lathia JD, Rich JN, Preferential Iron Trafficking Characterizes Glioblastoma Stem-like Cells., Cancer Cell. 28 (2015) 441–455. 10.1016/j.ccell.2015.09.002. [PubMed: 26461092]

[45]. Faurant C, From bark to weed: the history of artemisinin., Parasite. 18 (2011) 215–218. 10.1051/parasite/2011183215. [PubMed: 21894261]

[46]. O'Neill PM, Posner GH, A medicinal chemistry perspective on artemisinin and related endoperoxides., J. Med. Chem. 47 (2004) 2945–2964. 10.1021/jm030571c. [PubMed: 15163175]

[47]. Blank BR, Gonciarz RL, Talukder P, Gut J, Legac J, Rosenthal PJ, Renslo AR, Antimalarial Trioxolanes with Superior Drug-Like Properties and In Vivo Efficacy., ACS Infect. Dis. 6 (2020) 1827–1835. 10.1021/acsinfecdis.0c00064. [PubMed: 32369341]

[48]. Watson PA, Ellwood-Yen K, King JC, Wongvipat J, Lebeau MM, Sawyers CL, Context-dependent hormone-refractory progression revealed through characterization of a novel murine prostate cancer cell line., Cancer Res. 65 (2005) 11565–11571. 10.1158/0008-5472.CAN-05-3441. [PubMed: 16357166]

[49]. Nguyen HG, Conn CS, Kye Y, Xue L, Forester CM, Cowan JE, Hsieh AC, Cunningham JT, Truillet C, Tameire F, Evans MJ, Evans CP, Yang JC, Hann B, Koumenis C, Walter P, Carroll PR, Ruggero D, Development of a stress response therapy targeting aggressive prostate cancer., Sci. Transl. Med. 10 (2018). 10.1126/scitranslmed.aar2036.

[50]. Zhang Z, Connolly PJ, Lim HK, Pande V, Meerpoel L, Teleha C, Branch JR, Ondrus J, Hickson I, Bush T, Luistro L, Packman K, Bischoff JR, Ibrahim S, Parrett C, Chong Y, Gottardis MM, Bignan G, Discovery of JNJ-63576253: A Clinical Stage Androgen Receptor Antagonist for F877L Mutant and Wild-Type Castration-Resistant Prostate Cancer (mCRPC)., J. Med. Chem. 64 (2021) 909–924. 10.1021/acs.jmedchem.0c01563. [PubMed: 33470111]

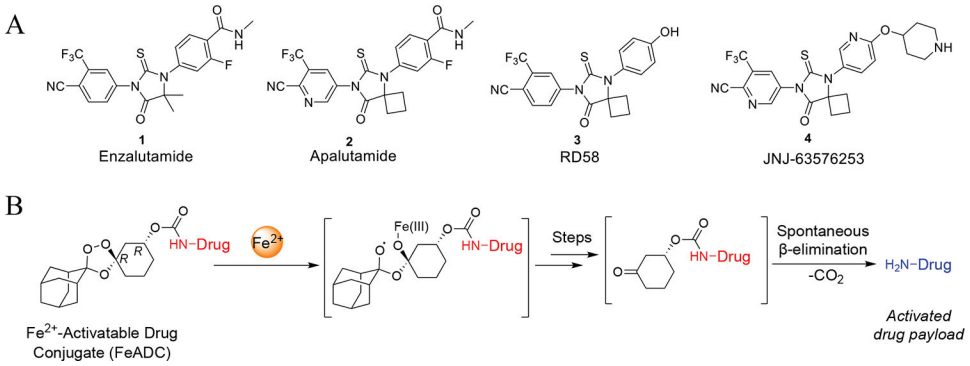

Figure 1.

(**A**) Structures of second- and third-generation antiandrogens. (**B**) Structure of a prototypical FeADC and the mechanism of traceless drug release following reaction with ferrous iron. Some steps omitted for clarity.

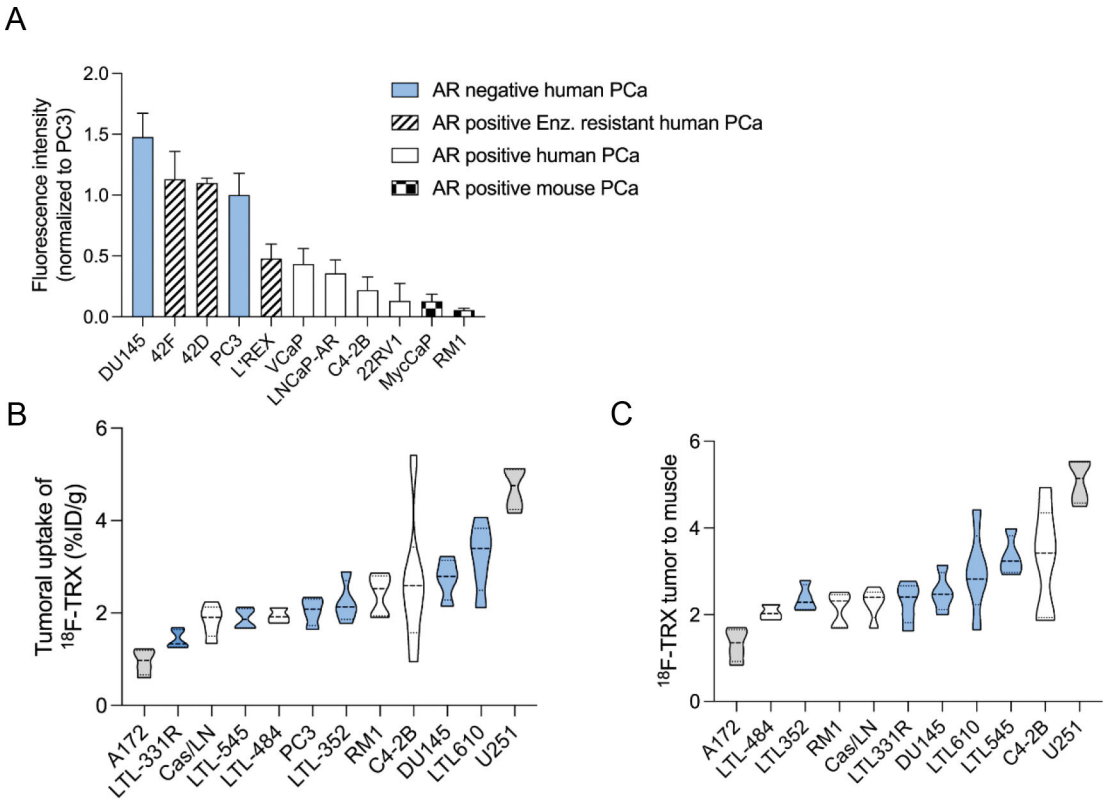

Figure 2.

Survey of cellular and tumoral Fe^{2+} levels in prostate cancer models. (**A**) *In vitro* data showing relative Fe^{2+} levels in multiple human and mouse prostate cancer cell lines using SiRhoNox. All data are normalized to Fe^{2+} levels in PC3 cells. (**B**) Tumoral Fe^{2+} levels as measured by uptake of ^{18}F-TRX *in vivo*. (**C**) Biodistribution data showing ratio of ^{18}F-TRX uptake in muscle and tumor tissue. Prostate adenocarcinoma models are shown in white, AR negative prostate cancer is shown in blue and low- and high-responding glioma models (for reference) are shown in grey.

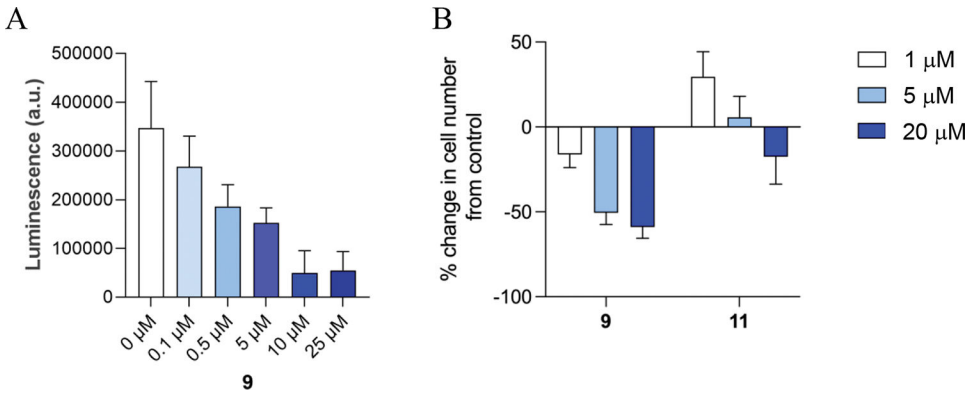

Figure 3.

In vitro antiproliferation studies with **9** and its bioisosteric, non-peroxidic control **11**. **(A)** LNCaP-AR cells are sensitive to **9** at low micromolar doses. **(B)** Comparison of antiproliferative effects of **9** and its bioisosteric, non-peroxidic control **11** at equimolar doses.

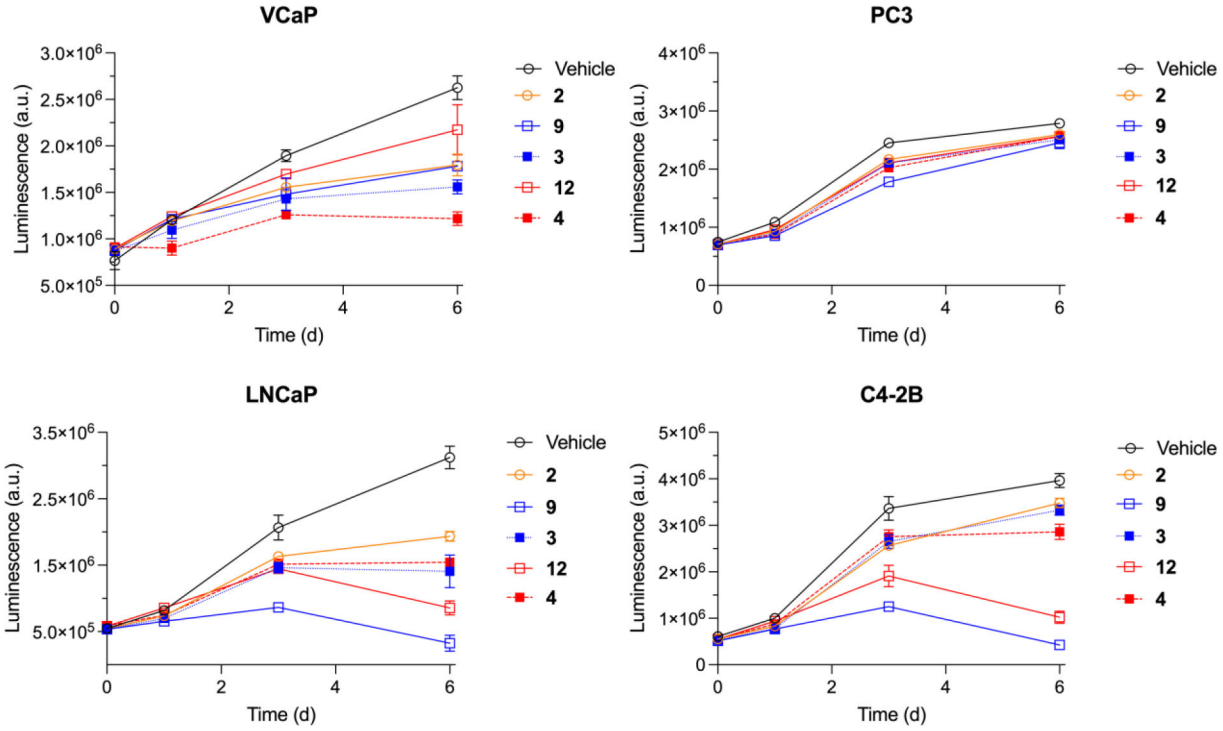

Figure 4.

Antiproliferative effects of antiandrogen FeADCs and controls against mCRPC model cell lines. Antiproliferative effects of test compounds over 6 days in three AR-positive (LNCaP, C4–2B and VCAP) and one AR-negative (PC3) human prostate cancer cell lines. All compounds tested at 5 μM.

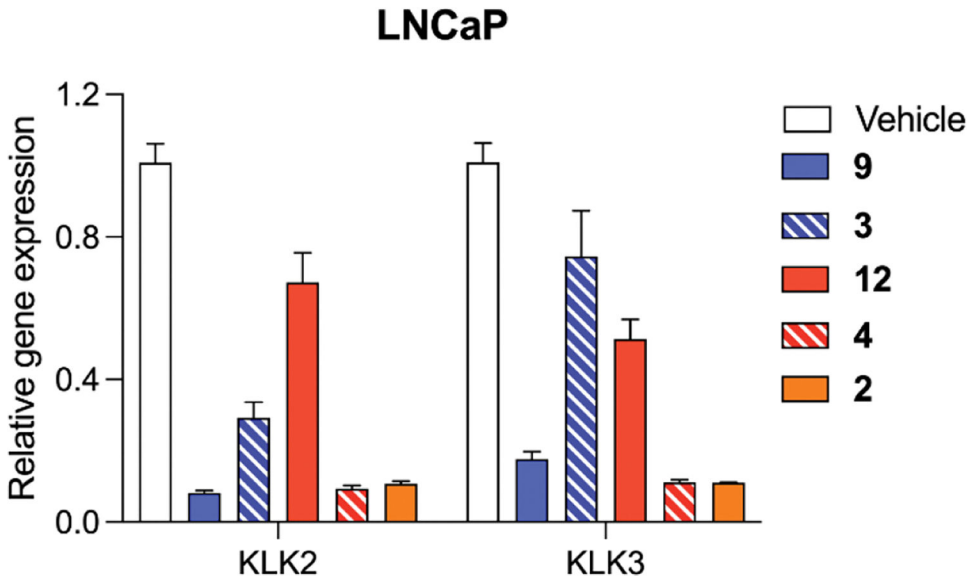

Figure 5.

Real-time PCR data showing antiandrogen FeADCs **9** and **12** suppress the expression of AR target genes KLK2 and KLK3 to a greater (for **9**) and lesser (for **12**) extent than their respective antiandrogen payloads **3** and **4**. Apalutamide (**2**) is a positive control. All compounds were administered at 5 μM and rt-PCR data collected at 24 hours post drug exposure.

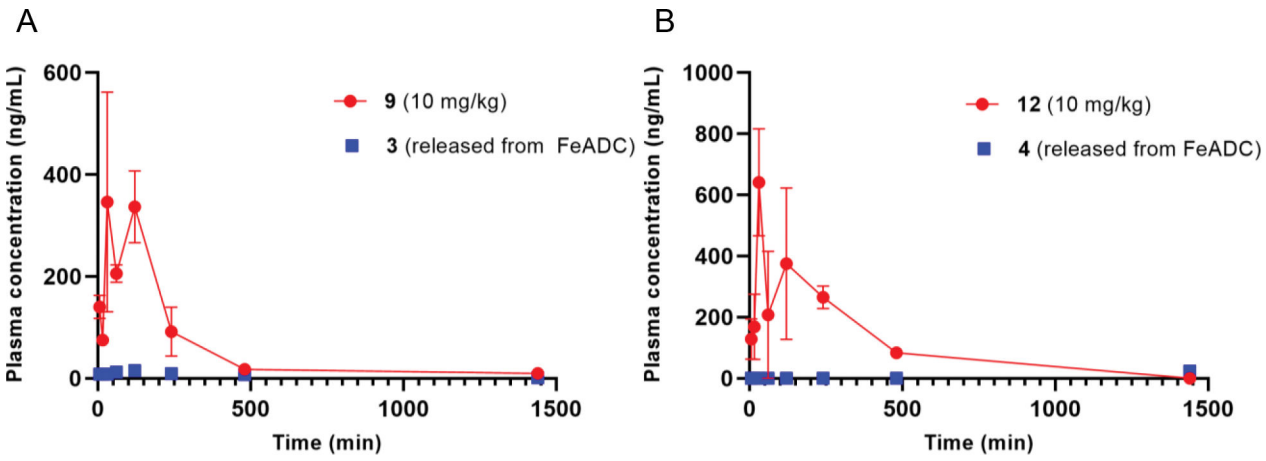

Figure 6.

(A) PK profile of **9** and released **3** in plasma following a single 10 mg/kg IP dose in NSG mice (n = 9). **(B)** PK profile of **12** and released **4** in plasma following a single 10 mg/kg IP dose to healthy NSG mice in plasma (n = 6).

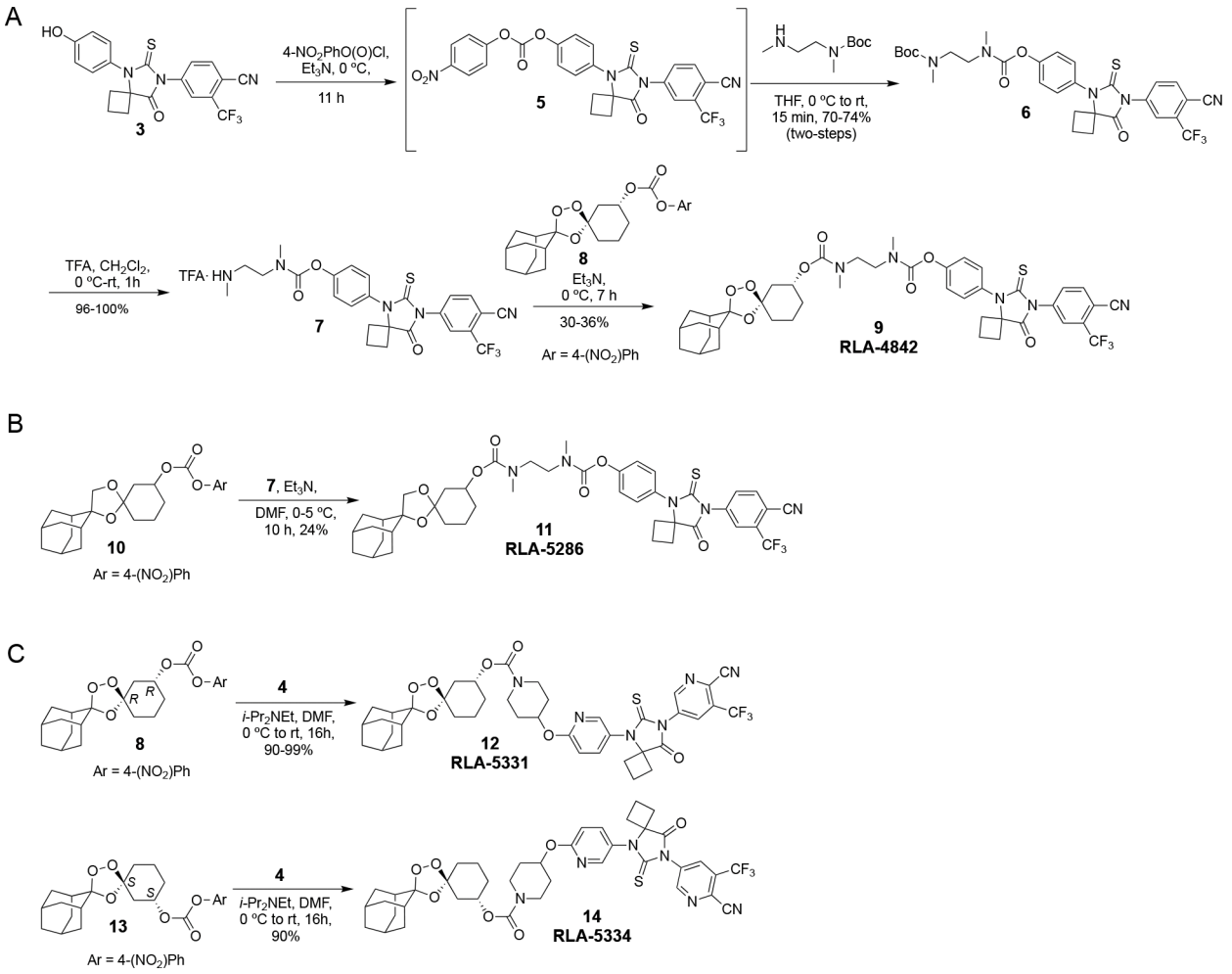

Scheme 1.

(A) Synthetic route to di-carbamate FeADC **9**. **(B)** Synthesis of non-peroxidic control compound **11**. (**C**) Synthesis of FeADCs **12** and **14** derived from (*R, R*) and (*S, S*) forms of the TRX moiety.

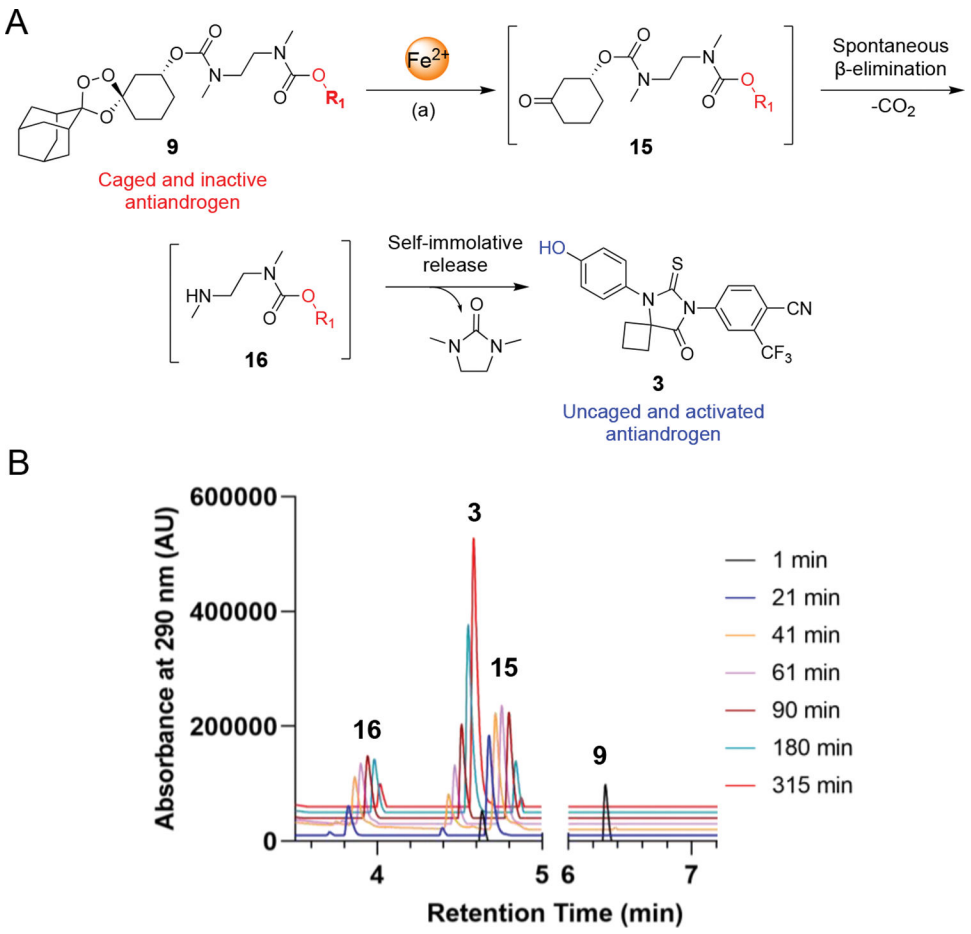

Scheme 2.

(A) Expected mechanism of payload release from **9** upon reaction with Fe^{2+}. **(B)** UPLC chromatograms showing the expected fragmentation intermediates **15, 16** and released payload **3**, following reaction of **9** with $FeSO_4 \cdot 7H_2O$, Tris-HCl pH 7.5/DMSO (1:1) at 37 °C.

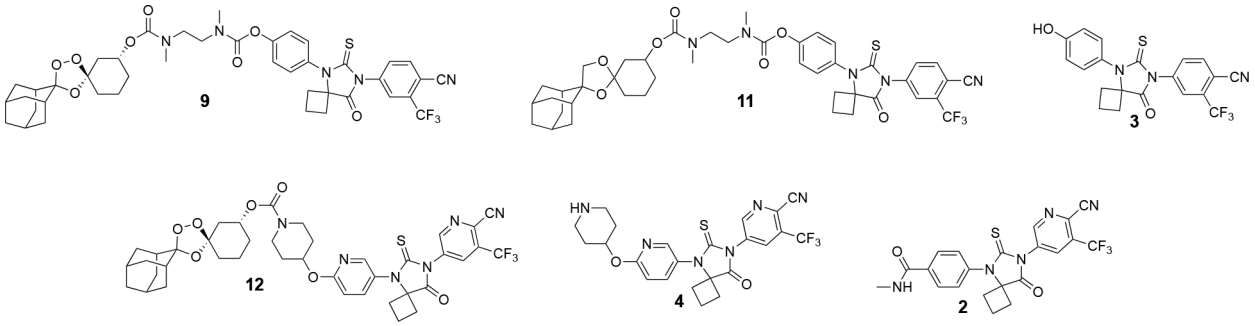

Chart 1.

Structures of FeADCs **9** and **12**, their respective antiandrogen payloads **3** and **4**, and positive and negative controls **2** and **11**.

Table 1:

In vitro ADME data for antiandrogen FeADCs.

Species	Compound	$T_{1/2}$ (min)[b]	CL_{int}[b] (μL/min/mg protein)	kinetic solubility (pH 7.4) μM[c]
Mouse	Verapamil	3.3	419.8	N/A
	12	48.2 ± 8.3	28.8 ± 4.9	<0.4
	14	34.5 ± 10.3	40.2 ± 12.0	<0.4
Human	**9**	53.4 ± 10.4	25.9 ± 5.1	2.3

[b] Stability of conjugates **12**, **14** and **9** in mouse liver microsomes (MLM) or human liver microsomes (HLM) represented as half-life or intrinsic clearance.

[c] Solubility measured by automated miniaturized shake flask method, in phosphate buffered saline, pH 7.4.

Table 2:

Selected plasma PK parameters for **9**, **12**, and apalutamide (**2**) following a single 10 mg/kg IP dose to NSG mice. Bioanalysis of plasma samples performed by Integrated Analytical Solutions, Berkeley, CA.

Compound	T_{max} (hr)	C_{max} (ng/mL)	AUC_{last} (hr•ng/mL)
2	4	4330	4494658
9	0.5	346	81091
12	0.5	641	158390